

# SMALL-SCALE DYNAMO SIMULATIONS: MAGNETIC FIELD AMPLIFICATION IN EXPLODING GRANULES AND THE ROLE OF DEEP AND SHALLOW RECIRCULATION

M. REMPEL<sup>1</sup>  
(Received; Accepted)

<sup>1</sup>High Altitude Observatory, NCAR, P.O. Box 3000, Boulder, Colorado 80307, USA

## ABSTRACT

We analyze recent high resolution photospheric small-scale dynamo simulations that were computed with the MURaM radiative MHD code. We focus the analysis on newly forming downflow lanes in exploding granules since they show how weakly magnetized regions in the photosphere (center of granules) evolve into strongly magnetized regions (downflow lanes). We find that newly formed downflow lanes exhibit initially mostly a laminar converging flow that amplifies the vertical magnetic field embedded in the granule from a few 10 G to field strengths exceeding 800 G. This results in extended magnetic sheets that have a length comparable to granular scales. Field amplification by turbulent shear happens first a few 100 km beneath the visible layers of the photosphere. Shallow recirculation transports the resulting turbulent field into the photosphere within minutes, after which the newly formed downflow lane shows a mix of strong magnetic sheets and turbulent field components. We stress in particular the role of shallow and deep recirculation for the organization and strength of magnetic field in the photosphere and discuss the photospheric and sub-photospheric energy conversion associated with the small-scale dynamo process. While the energy conversion through the Lorentz force depends only weakly on the saturation field strength (and therefore deep or shallow recirculation), it is strongly dependent on the magnetic Prandtl number. We discuss the potential of these findings for further constraining small-scale dynamo models through high resolution observations.

*Keywords:* Sun: granulation; Sun: magnetic fields; Sun: photosphere; magnetohydrodynamics (MHD); radiative transfer; methods: numerical

## 1. INTRODUCTION

Observations suggest that small-scale magnetic field in the solar photosphere is mostly independent from the strength of nearby network field (Ishikawa & Tsuneta 2009; Lites 2011; Lamb et al. 2014) as well as independent of the solar cycle (Buehler et al. 2013; Lites et al. 2014). This supports the view that the origin of small-scale magnetism is due to a small-scale dynamo that operates independently from the large-scale dynamo responsible for the solar cycle. A small-scale dynamo as origin of the quiet sun magnetic field was first suggested by Petrovay & Szakaly (1993) and numerical simulations in incompressible setups conducted by Cattaneo (1999) further supported that concept. Stein et al. (2003) pointed out that there is only very little local re-circulation in the photosphere and they suggested that even the small-scale dynamo has to operate throughout the convection zone on a global scale. Vögler & Schüssler (2007) presented the first realistic solar MHD simulations with radiative transfer and demonstrated that an excited small-scale dynamo can exist in the photosphere in spite of low local recirculation (they used a bottom boundary condition that did not allow for a Poynting flux in upflows, which essentially isolates the photosphere from the rest of the convection zone). However, the saturation field strength ( $\langle |B_z| \rangle (\tau = 1) \approx 25$  G) fell short of observations by about a factor of 2 – 3 (Danilovic et al. 2010). Rempel (2014) presented models with reduced numerical diffusivities and different bottom boundary conditions that emulate the presence of a deep magnetized convection zone. It was found that just reducing numerical diffusivities alone does not increase the saturation field strength sufficiently beyond the values found by Vögler & Schüssler (2007), instead the bottom boundary condition plays a key-role. A saturation field strength consistent with observational constraints (Rempel 2014; Danilovic et al. 2016) requires a setup that has either complete recirculation within the simulation domain (closed bottom boundary), or a bottom boundary that emulates the presence of a deep magnetized convection zone through the presence of horizontal magnetic field in upflows as previously conjectured by

Stein et al. (2003). Solutions that are consistent with observations ( $\langle |B_z| \rangle (\tau = 1) \approx 60 - 80$  G) require a subsurface RMS field strength that is about  $0.5 - 1 B_{\text{eq}}$ , with the equipartition field strength  $B_{\text{eq}} = \sqrt{4\pi\varrho} V_{\text{RMS}}$ , (Rempel 2014). Such subsurface field strength values are consistent with those found in deep seated small-scale dynamo simulations that reach to the base of the solar convection zone and therefore account for full recirculation, but do not include the upper layers of the convection zone (Hotta et al. 2015).

Overall the above research suggests that the efficiency of recirculation plays a central role in determining the photospheric saturation values of the small-scale dynamo, i.e. quiet sun magnetism is not due to a “local” dynamo operating in the photosphere, it is more a reflection of a deep seated small-scale dynamo where the deeper convection zone plays a key role in shaping the photospheric appearance of small-scale magnetism.

Since both resolution (which in combination with either explicit or implicit magnetic diffusivity determines the supercriticality of the dynamo during its kinematic phase) and boundary conditions influence the saturation field strength of a dynamo simulation, it is not surprising that different models do not necessarily show comparable saturation levels. For example Kitiashvili et al. (2015, see, Figure 16 therein) found photospheric values of  $\langle |B_z| \rangle$  and  $\langle B_h \rangle$  in the 10 – 20 G range, which is lower than Vögler & Schüssler (2007); Khomenko et al. (2017) found a photospheric saturation field strength of  $\langle |\mathbf{B}| \rangle \approx 100$  G, which is about half way between the results of Vögler & Schüssler (2007) and Rempel (2014). The role of resolution and boundary conditions was not further investigated in Kitiashvili et al. (2015) and Khomenko et al. (2017), which makes a cross-comparison of all these models challenging.

In addition to the role of recirculation, the role of the magnetic Prandtl number ( $P_m$ ) on the dynamo efficiency has been studied in great detail. The latter is of particular interest for the solar dynamo since  $P_m$  reaches values as low as  $10^{-5}$  in the photosphere. Schekochihin et al. (2005, 2007) considered simulations of forced turbulence to study the onset of dynamo action in the kinematic phase. Schekochihin et al. (2007) and Isakov et al. (2007) concluded that the fluctuation dynamo does exist also in the low  $P_m$  regime, but with a critical magnetic Reynolds number about a factor 3 larger compared to the high  $P_m$  regime. While these direct numerical simulations could not achieve  $P_m$  values lower than 0.1 to 0.01, the asymptotic limit of very low  $P_m$  has been studied in a more idealized model by Boldyrev & Cattaneo (2004). They found that small-scale dynamo action remains possible for rough velocity fields (low  $P_m$ ), while the critical magnetic Reynolds number is larger by a factor of a few (see also the review of Tobias et al. (2013) for further discussion). Studies of the role of  $P_m$  for the saturated small-scale dynamo were conducted by Brandenburg (2011, 2014). They found that the dynamo efficiency (ratio of work against Lorentz force and the available driving through forcing terms) depends upon the magnetic Prandtl number, suggesting that  $P_m$  strongly influences the ratio of resistive to viscous energy dissipation, with resistive dissipation being dominant in the low  $P_m$  regime.

$P_m$  dependence studies are much more challenging for convective dynamo setups representing conditions in the solar photosphere. Bushby & Favier (2014) considered convective small-scale dynamos on scales of granulation and meso-granulation. They used explicit viscosity and magnetic resistivity and found excited dynamos only for  $P_m$  values larger than 0.5. Many of the recent solar-like simulations rely at least partially on numerical diffusivities using either implicit or explicit subgrid-scale models, which makes a quantification of  $P_m$  challenging. Since numerical diffusivities can vary substantially based on the local structure of velocity and magnetic field,  $P_m$ , if defined locally, is highly intermittent and varies substantially throughout the simulation domain. Pietarila Graham et al. (2010) analyzed dynamo simulations similar to those presented by Vögler & Schüssler (2007) and defined a global numerical  $P_m$  based on the kinetic and magnetic energy Taylor microscale and found values in the 0.8 – 2 range. Thaler & Spruit (2015) found an excited small-scale dynamo for  $P_m = 5$  in their setup (about neutral growth for  $P_m = 2$ ), where  $P_m$  was defined as a pre-factor that scales magnetic hyperdiffusivity relative to hyperviscosity (which can be also considered a global definition of  $P_m$ ). In contrast to that Kitiashvili et al. (2015) and Khomenko et al. (2017) considered local definitions of  $P_m$  and found that those values vary substantially by several orders of magnitude. Most of the induction as well as magnetic energy density was however associated with local  $P_m$  slightly smaller than 1.

In the first part of this paper we present a study that aims at identifying observables that could help to further constrain the role of recirculation. To this end we analyze and compare 2 simulations from Rempel (2014) that have the same numerical resolution, but differ in their treatment of the bottom boundary condition. In particular we focus on newly forming downflow lanes in exploding granules that show how the most weakly magnetized regions in the photosphere (center of granules) evolve into the most strongly magnetized regions (downflow lanes). That process is in particular sensitive to the “seed field” that is present in the center of granules and brought into the visible layers of the photosphere through recirculation. While the outer regions of granules show mostly turbulent field that is transported back into the photosphere due to local recirculation (upflow/downflow mixing), the centers of granules are expected to exhibit field that is brought up from deeper layers of the photosphere. We study primarily exploding granules since they provide the most undisturbed view on the field amplification process, the described picture is

however representative for the photosphere as a whole. In the second part of paper we focus on the photospheric and sub-photospheric energy conversion and discuss how the dynamo efficiency depends on shallow/deep recirculation as well as the magnetic Prandtl number. In particular we present here an extension of the work by [Rempel \(2014\)](#) by considering also models that use "numerical"  $P_m$  with values far from unity. We focus here in particular on the findings of [Brandenburg \(2011, 2014\)](#) on the role of  $P_m$  for the energy dissipation in a saturated dynamo.

## 2. SIMULATION DATA

We analyze a photospheric small-scale dynamo simulation that was already presented in [Rempel \(2014\)](#). We focus on the model ‘O4a’ with 4 km grid spacing in a 6.144 Mm wide and 3.072 Mm deep domain. The photosphere is located about 700 km beneath the top boundary. The setup reaches at an optical depth of unity a mean vertical field strength of about  $\langle |B_z| \rangle \sim 85$  G, which corresponds to  $\langle |\mathbf{B}| \rangle \sim 165$  G, and  $B_{\text{RMS}} \sim 250$  G. In the following we refer to this simulation as  $\text{SSD}_{\text{Deep}}$ . The saturation field strength of 85 G is moderately stronger than the value of 60 G inferred from Hinode observations [Danilovic et al. \(2016\)](#) through forward modeling of spectro-polarimetric signatures. Recently del Pino Aleman et al. (2018, in prep.) found that the magnetization of a [Rempel \(2014\)](#) model with a surface mean field strength of about 160 G is consistent with Hanle-depolarization observed in the Sr I 460.7 nm line. The model  $\text{SSD}_{\text{Deep}}$  uses an open bottom boundary condition that mimics a deep magnetized convection zone by allowing for the presence of horizontal magnetic field in upflow regions (deep recirculation). The boundary condition mirrors the magnetic field vector from the lowermost domain cells into the boundary cells, which does result in upflow regions in a horizontal magnetic field that is organized on a scale comparable to convection cells near the bottom boundary, but has no preferred direction or net horizontal flux (see, [Rempel 2014](#), for further detail). In order to highlight the role of this deep recirculation we analyze a second model that has a similar setup as the model ‘Z8’ presented in [Rempel \(2014\)](#), but we recomputed a 1 hour sequence with a grid spacing of 4km. This model uses an open bottom boundary that imposes  $\mathbf{B} = 0$  G in inflow regions. The photospheric saturation field strength is around  $\langle |B_z| \rangle \sim 45$  G, which corresponds to  $\langle |\mathbf{B}| \rangle \sim 90$  G, and  $B_{\text{RMS}} \sim 140$  G. This model relies completely on local recirculation within the simulation domain, similar to [Vögler & Schüssler \(2007\)](#), we refer to this model in the following as  $\text{SSD}_{\text{Shallow}}$ .

## 3. RESULTS

### 3.1. Photospheric evolution

We select in the simulation  $\text{SSD}_{\text{Deep}}$ , which covers during its saturated phase about 2 hours of temporal evolution, 4 exploding granules. Figure 1 shows the first example, the other 3 examples can be found in the Appendix A. We present top to bottom 4 snapshots spaced about 130 seconds in time (due to the variable numerical time step the time spacing is not equidistant). Left panels show the evolution of bolometric intensity for a vertical ray direction, middle panels the vertical velocity and right panels the vertical component of the magnetic field on the  $\tau = 1$  level. In the first snapshot Figure 1(a,b,c), the intensity image shows already a central darkening of the granule, the vertical velocity in the center of the granule starts to show a weak downflow. The granule is filled with a weak vertical magnetic field of a few 10 G strength (see also Figure 3c) that is organized on a scale comparable to the granule itself. The next snapshot Figure 1(d,e,f) 132 seconds later shows now a well established downflow reaching 4 km/s in amplitude and hosting a sheet of strong vertical magnetic field. The sheet shows a mix of polarities, since the initial field present in the granule was not uni-polar. The intensity image shows some asymmetry of the newly formed downflow, with a brighter and sharper upper edge (indicated by arrow), which is related to a stronger convective upflow on that side of the granule. In the following two snapshots it is this side of the downflow lane where we find turbulent magnetic field appearing at the edge of the adjacent granule (transported into the photosphere by the granular upflow). The turbulent field is eventually swept into the newly formed downflow lane and leads to a turbulent magnetic field within the downflow lane with an appearance similar to that found in well established downflow lanes.

While we focus the following analysis on the case presented in Figure 1, we present in the Appendix Figures 9, 10, and 11 three additional cases in order to highlight the robustness of the studied sequence of events.

The vertical cross-sections displayed in Figure 2 show more clearly the nature of the underlying flow pattern. The newly formed downflow lane in the exploding granule remains very shallow and reaches in depth only a few 100 km beneath the  $\tau = 1$  level. Horizontal flows in particular in panels (d) and (g) indicate the formation of a horizontal vortex roll parallel to the downflow lane. As first discovered by [Steiner et al. \(2010\)](#) such mostly horizontal vortex rolls lead to distinct features in the intensity of a granule similar to those presented in Figure 1. In addition to that the enhanced adjacent granular upflow transports magnetic field back into the photosphere that becomes first visible at the  $\tau = 1$  surface in the third snapshot (panels (g)-(i) of Figures 1 and 2). The appearance of this recirculated field is more turbulent in the later snapshots presented in panels (j) to (l).

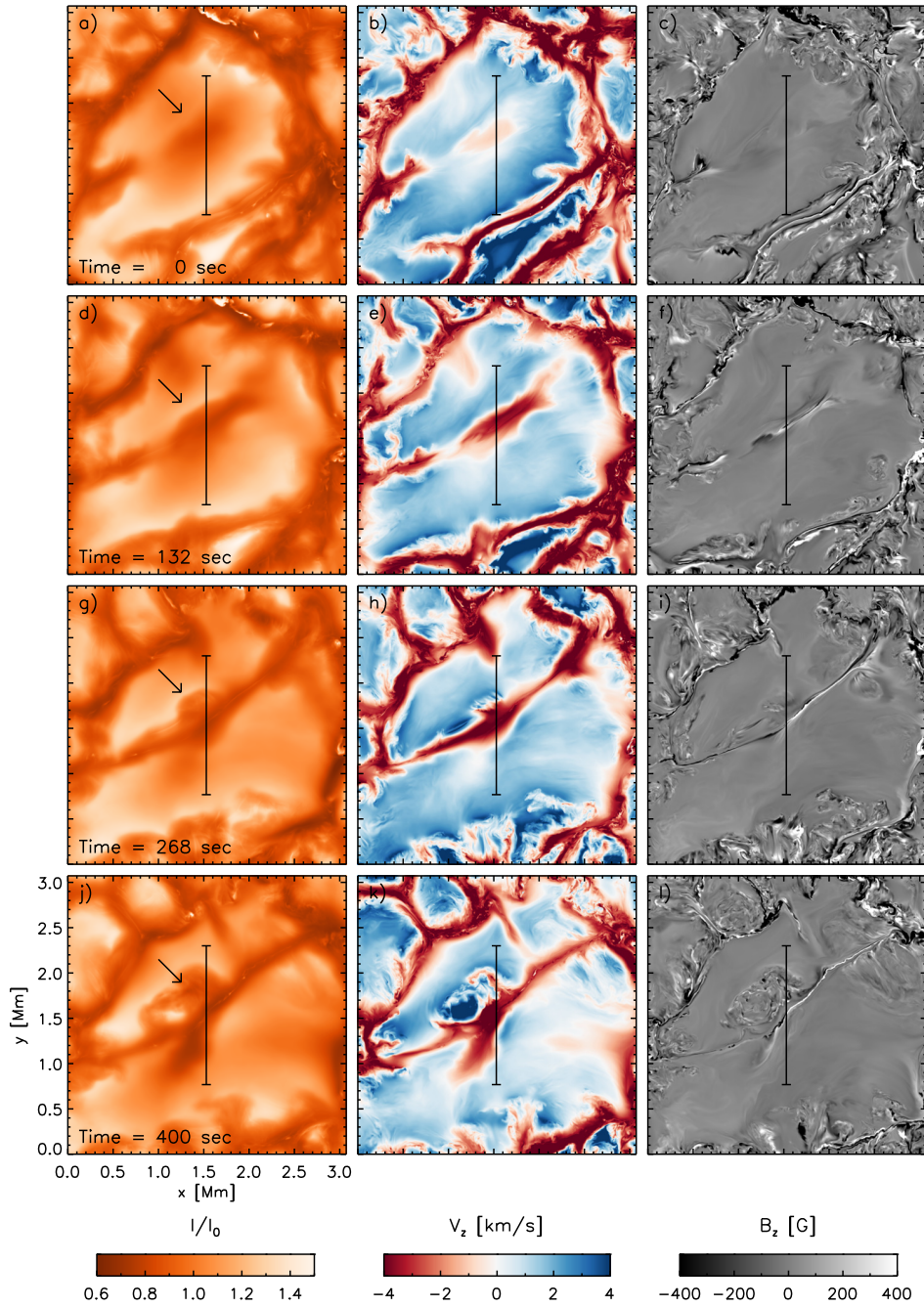


**Figure 1.** Evolution of bolometric intensity (left), vertical velocity (middle), and vertical magnetic field (right) in an exploding granule over a time span of about 400 seconds (top to bottom). The vertical velocity and magnetic field are extracted on the  $\tau = 1$  surface. The black line indicates the position of a vertical cut discussed further in Figure 2. An animation of this figure showing the temporal evolution over an extended time interval of 926 seconds is available.

Figure 3 presents the induction terms for the vertical magnetic field component evaluated on the  $\tau = 1$  surface. We compute here the induction terms using quantities extracted on the  $\tau = 1$  surface rather than computing the terms on constant height surfaces and extracting the result on the  $\tau = 1$  surface, since the former could be more easily accomplished based on observational data. We note that the difference is insignificant since the  $\tau = 1$  surface is not heavily distorted within the exploding granule (see Figure 2). We write the induction equation for the vertical magnetic field component as follows:



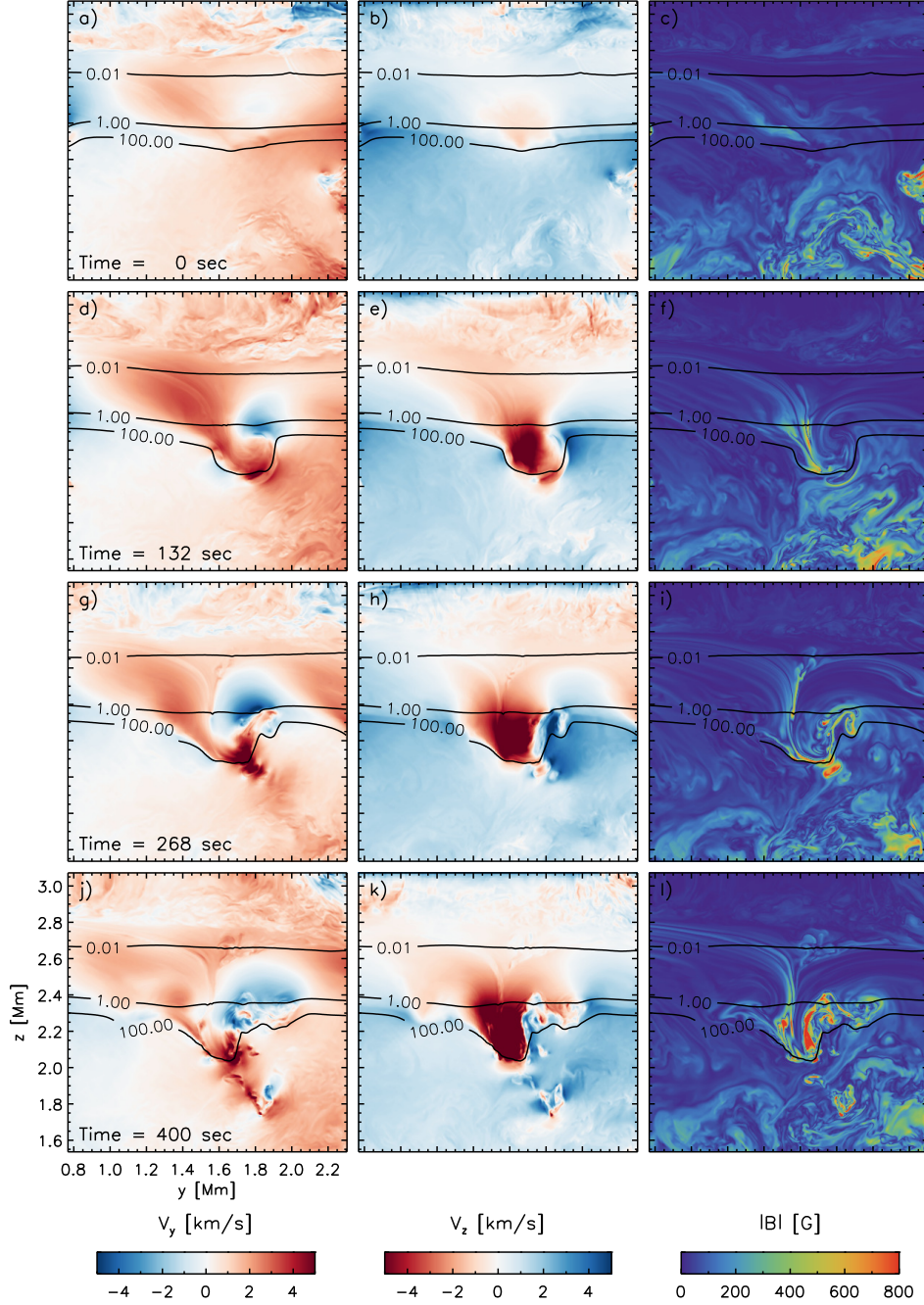


**Figure 2.** Quantities extracted along the vertical cut indicated in Figure 1. Horizontal flow velocity along the cut in the  $y$ -direction (left), vertical flow velocity (middle), and vertical field strength (right). We show top to bottom the same snapshots as in Figure 1. Black contours indicate the  $\tau$  levels of 100, 1, and 0.01.

$$\frac{DB_z}{Dt} = \underbrace{-B_z \left( \frac{\partial v_x}{\partial x} + \frac{\partial v_y}{\partial y} \right)}_{\text{convergence/divergence}} + \underbrace{B_x \frac{\partial v_z}{\partial x} + B_y \frac{\partial v_z}{\partial y}}_{\text{shear}} \quad (1)$$

Note that this decomposition of terms is different from the usual separation of compression and stretching terms, which would involve a contribution from  $B_z \partial v_z / \partial z$  that cancels out. We prefer this decomposition since it clearly separates field amplification of existing vertical field due to horizontally convergent flows from the induction due to shear acting on horizontal field components. We present the divergence/convergence and shear terms in the left and

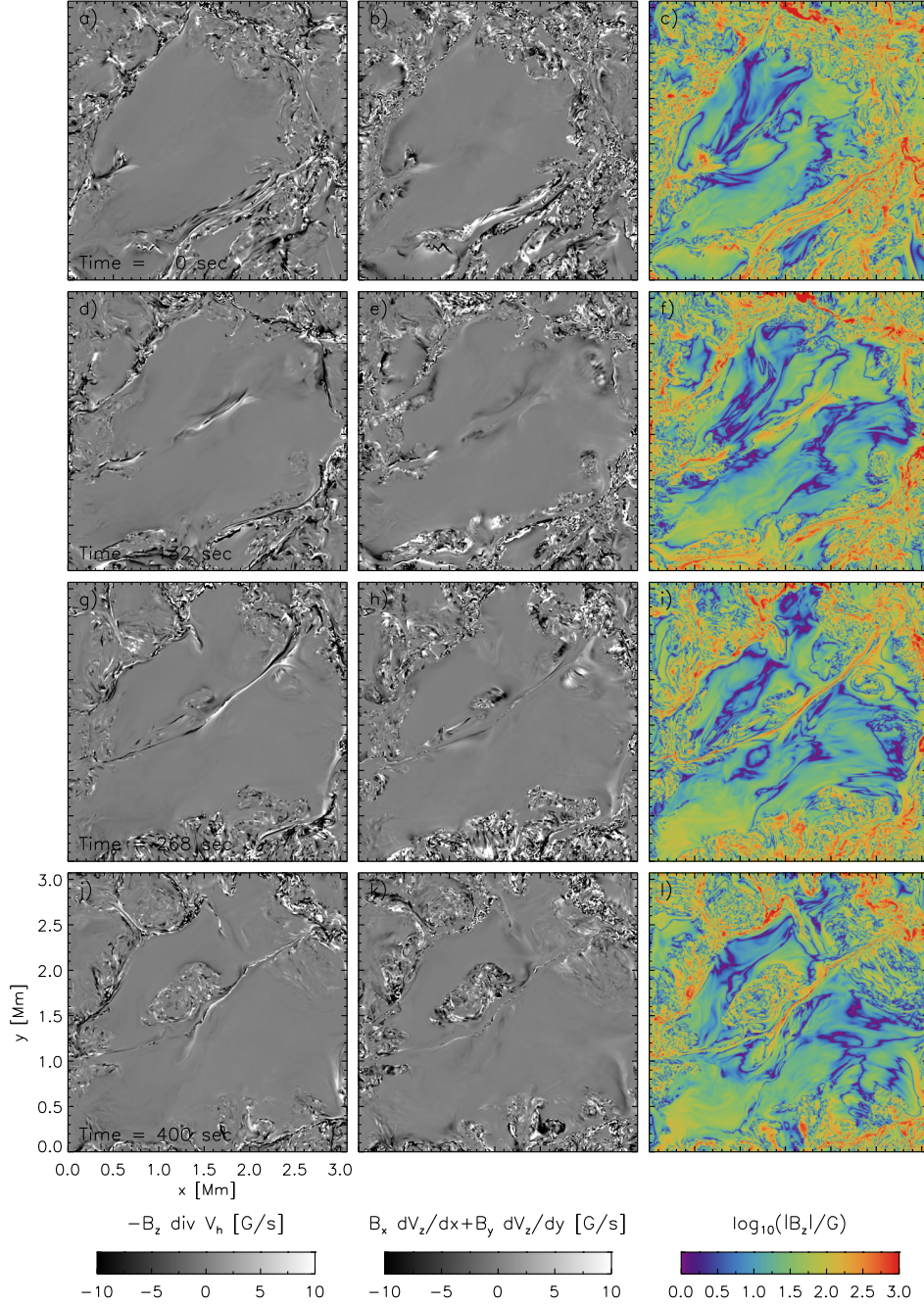


**Figure 3.** Induction terms for vertical magnetic field component from horizontal flow divergence (left) and shear (middle). The right panels show the vertical field strength on a log scale. We show top to bottom the same snapshots as in Figure 1. All quantities are extracted on the  $\tau = 1$  surface.

middle panels of Figure 3 together with the vertical field strength on a logarithmic scale in the right panels. The convergence term dominates the early phase of the field amplification (first two snapshots), the shear term starts dominating as soon as magnetic field with a more turbulent nature appears at the edge of the granule (last two snapshots). Overall this indicates that a newly formed downflow lane in the photosphere remains initially mostly laminar. The granular seed field is amplified due to strong horizontal convergence of flows, which leads to induction rates exceeding  $10 \text{ G s}^{-1}$ . Starting with a granular seed field on the order of a few 10 G this term produces a field exceeding 800 G in the downflow lane at  $\tau = 1$  in a few minutes of time. Field amplification by shear (producing field with a more turbulent appearance) happens beneath the visible layers of the photosphere; however, the rather shallow



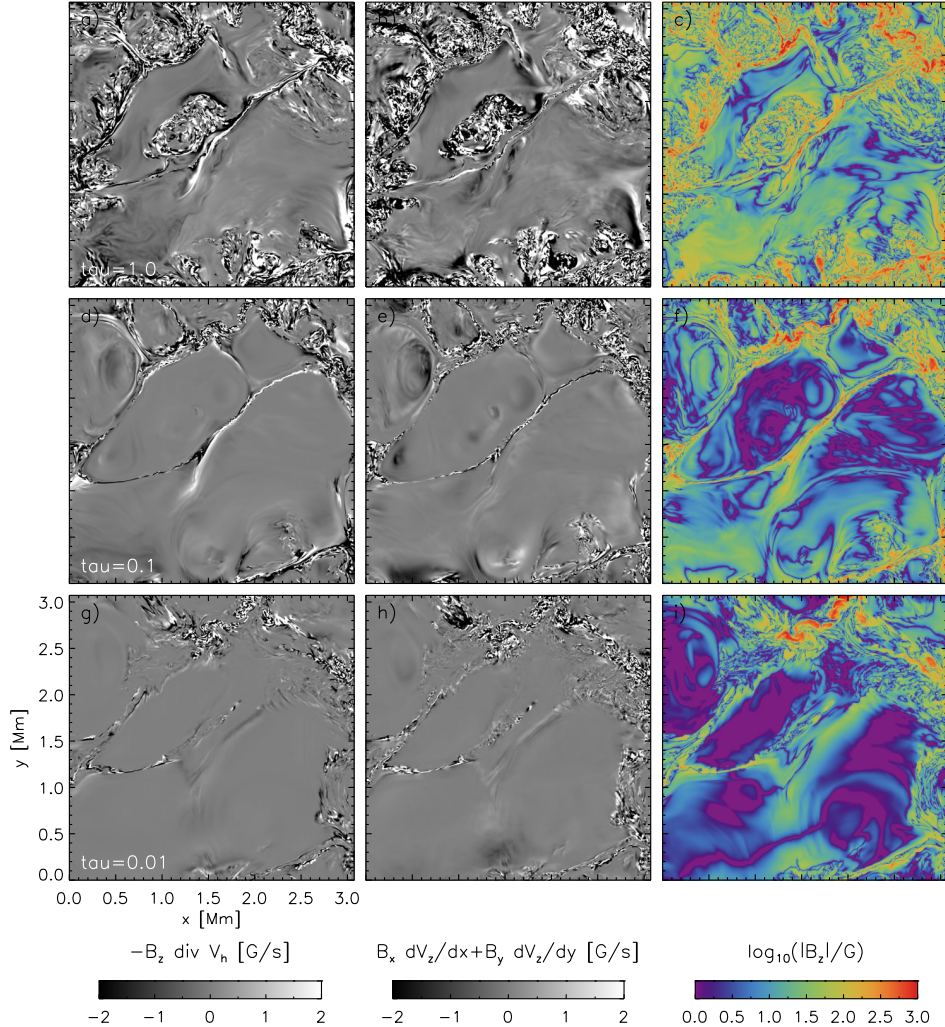


**Figure 4.** Height dependence of the induction terms shown in Figure 3. We show top to bottom the  $\tau$  surfaces of 1, 0.1, and 0.01 for the last snapshot at  $t = 400$  seconds.

recirculation transports that field back into the visible photosphere on a time scale of minutes. Most of this turbulent field remains in the deep photosphere as indicated in Figure 4, where we show the last snapshot of Figure 3 for the  $\tau$  levels of 1, 0.1, and 0.01.

In Figure 5 we present quantities similar to those in Figure 1 for the simulation  $\text{SSD}_{\text{Shallow}}$  that imposes  $\mathbf{B} = 0$  G in inflow regions at the bottom boundary. While we do find a similar series of events, the overall field strength is about a factor of 1.5 – 2 lower. We find a much less pronounced sheet-like magnetic field concentration in the newly forming downflow lane, both, in terms of strength as well as extent. Figure 6 shows the vertical and horizontal field strength on the  $\tau = 1$  level for the simulations  $\text{SSD}_{\text{Deep}}$  (top panels) and  $\text{SSD}_{\text{Shallow}}$  (bottom panels). In both cases we show the time snapshot corresponding to Figures 1g)-i) and 5g)-i), i.e.  $t = 268$  and 288 seconds, respectively. We find that the less coherent sheet-like field concentrations in the simulation  $\text{SSD}_{\text{Shallow}}$  are due to a much weaker and less organized seed field in the center of the granules. Whereas the simulation  $\text{SSD}_{\text{Deep}}$  had a granular seed field in the 10 – 100 G range that is organized on scales comparable to the size of a granule,  $\text{SSD}_{\text{Shallow}}$  shows in the central portions of the granule field strength of less than 1 G and the granular seed field is dominated by small-scale field at the edge of granules that results from shallow recirculation of turbulent field. The subsequent amplification of that field leads to a weaker less coherent field in the downflow lanes.

In both setups upflow regions are dominated by horizontal field, which is a consequence of horizontal expansion. The average values for  $|B_z|$  ( $|B_h|$ ) in upflow regions at  $\tau = 1$  are about 50 (100) G for  $\text{SSD}_{\text{Deep}}$  and 30 (60) G for  $\text{SSD}_{\text{Shallow}}$ . Subsequent field amplification is more efficient for the vertical field component, leading to average values

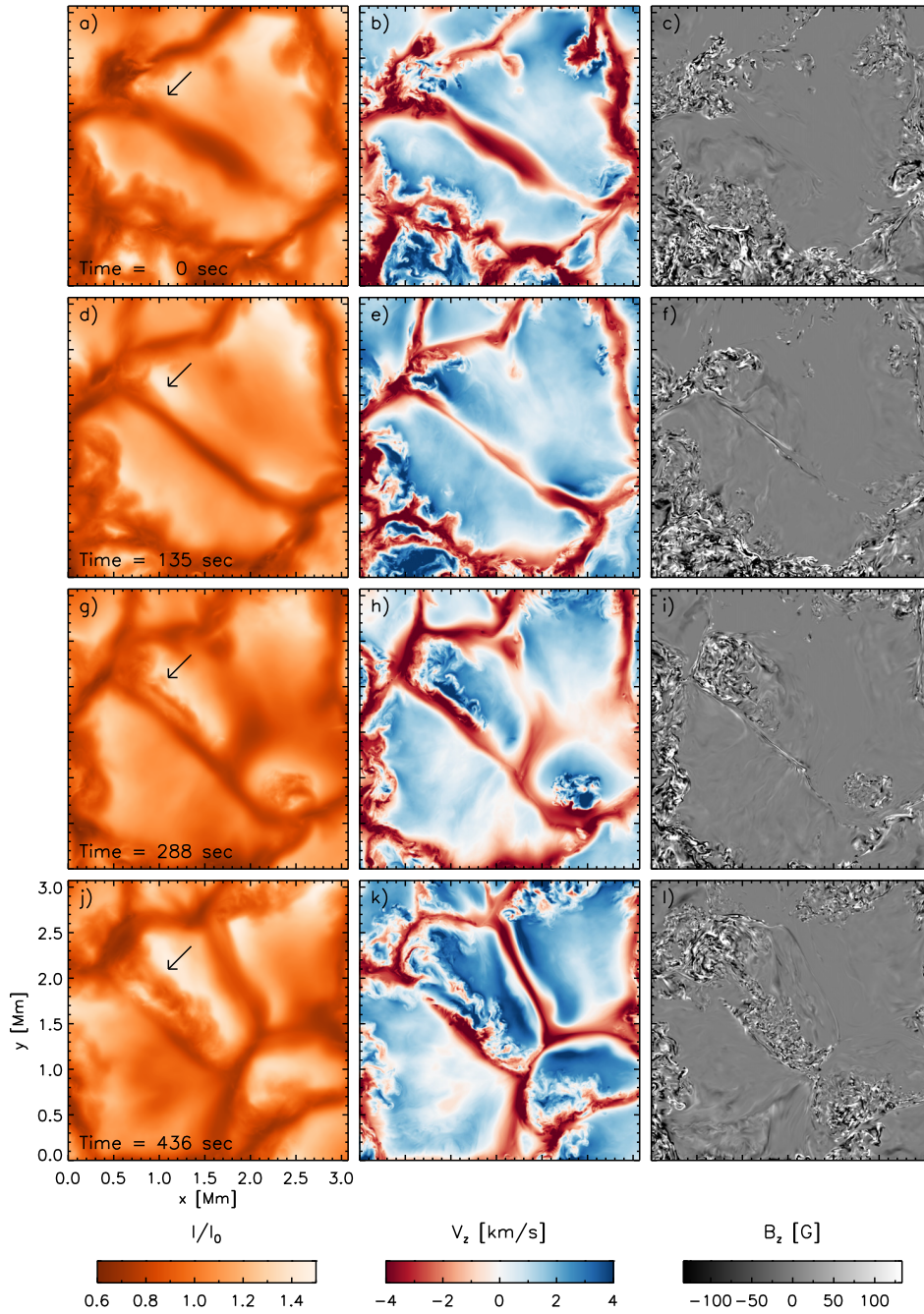


**Figure 5.** Same as Figure 1, but for the simulation  $\text{SSD}_{\text{Shallow}}$  ( $\mathbf{B} = 0$  G in upflows at the bottom boundary). While we do find a similar sequence of events as in the previous case, the overall field strength is about a factor of 3 lower. We see less pronounced sheet-like magnetic structures forming in the newly developing downflow lane.

in downflow regions of 130 (160) G and 65 (90) G, respectively. While the downflow regions of simulation  $\text{SSD}_{\text{Shallow}}$  are close to the expectation from an isotropic field distribution  $|B_h| = \sqrt{2}|B_z|$ , the average vertical field in  $\text{SSD}_{\text{Deep}}$  is stronger than the expectation from an isotropic distribution due to the presence of  $> 1$  kG field concentrations (see Rempel 2014, for further detail).

Overall the comparison of these two models demonstrates that the magnetic field present in the center of granules plays a crucial role in maintaining the quiet sun magnetic field. It provides the seed for further field amplification in the photosphere through a combination of concentration by convergent flows toward downflow lanes and subsequent amplification by turbulent shear beneath the visible layers of the photosphere. The magnetic field present in the center



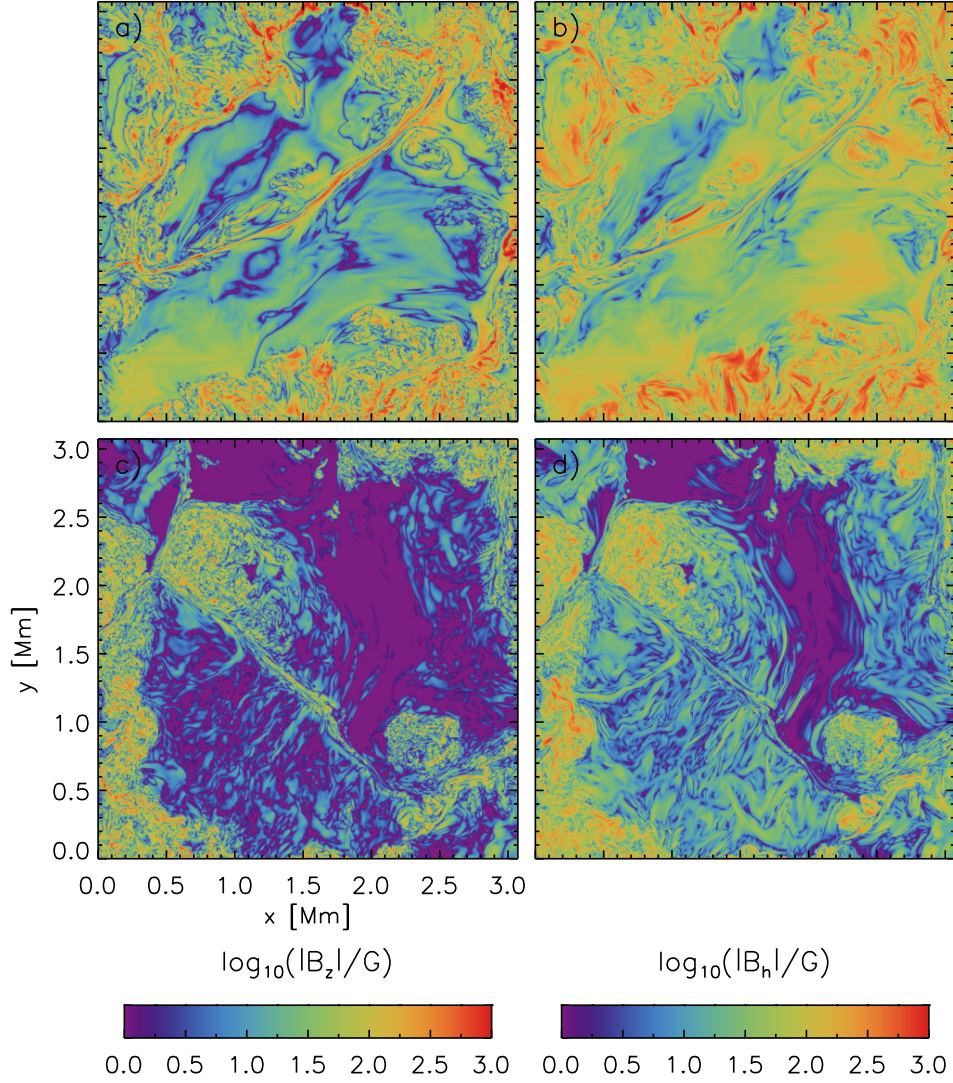


**Figure 6.** Comparison of photospheric magnetic field at  $\tau = 1$  in the simulation  $\text{SSD}_{\text{Deep}}$  (top) and  $\text{SSD}_{\text{Shallow}}$  (bottom). The panels on the left show  $|B_z|$ , the panels on the right  $|B_h|$ . The presented snapshots correspond to the snapshots displayed in Figures 1g)-i) and 5g)-i).

of granules is strongly linked to magnetic field in the deeper convection zone, which illustrates the important role for a deep seated recirculation in addition to a shallow photospheric recirculation. While the latter appears sufficient to maintain a dynamo, the former is required to push the saturation field strength to the levels implied by observations.

### 3.2. Photospheric and sub-photospheric energy conversion

In this section we discuss the energy conversion rates of the small scale dynamo in the upper most 1.5 Mm of the convection zone for the cases  $\text{SSD}_{\text{Deep}}$  and  $\text{SSD}_{\text{Shallow}}$ . To this end we focus on the kinetic and magnetic energy equations:

$$\frac{\partial}{\partial t} \left( \frac{1}{2} \rho v^2 \right) = \underbrace{-\nabla \cdot \left( \mathbf{v} \frac{1}{2} \rho v^2 \right)}_{Q_{\text{Kin}}} - \underbrace{\mathbf{v} \cdot (\nabla p - \rho \mathbf{g})}_{Q_{\text{Pres/Buo}}} + \underbrace{\mathbf{v} \cdot \frac{(\nabla \times \mathbf{B}) \times \mathbf{B}}{4\pi}}_{Q_{\text{Lorentz}}} + \mathbf{v} \cdot \mathbf{d}_v^{\text{NUM}} \quad (2)$$

$$\frac{\partial}{\partial t} \left( \frac{B^2}{8\pi} \right) = \underbrace{-\nabla \cdot \left( \frac{\mathbf{B} \times (\mathbf{v} \times \mathbf{B})}{4\pi} \right)}_{Q_{\text{Poynting}}} - \mathbf{v} \cdot \frac{(\nabla \times \mathbf{B}) \times \mathbf{B}}{4\pi} + \frac{1}{4\pi} \mathbf{B} \cdot \mathbf{d}_B^{\text{NUM}} \quad (3)$$

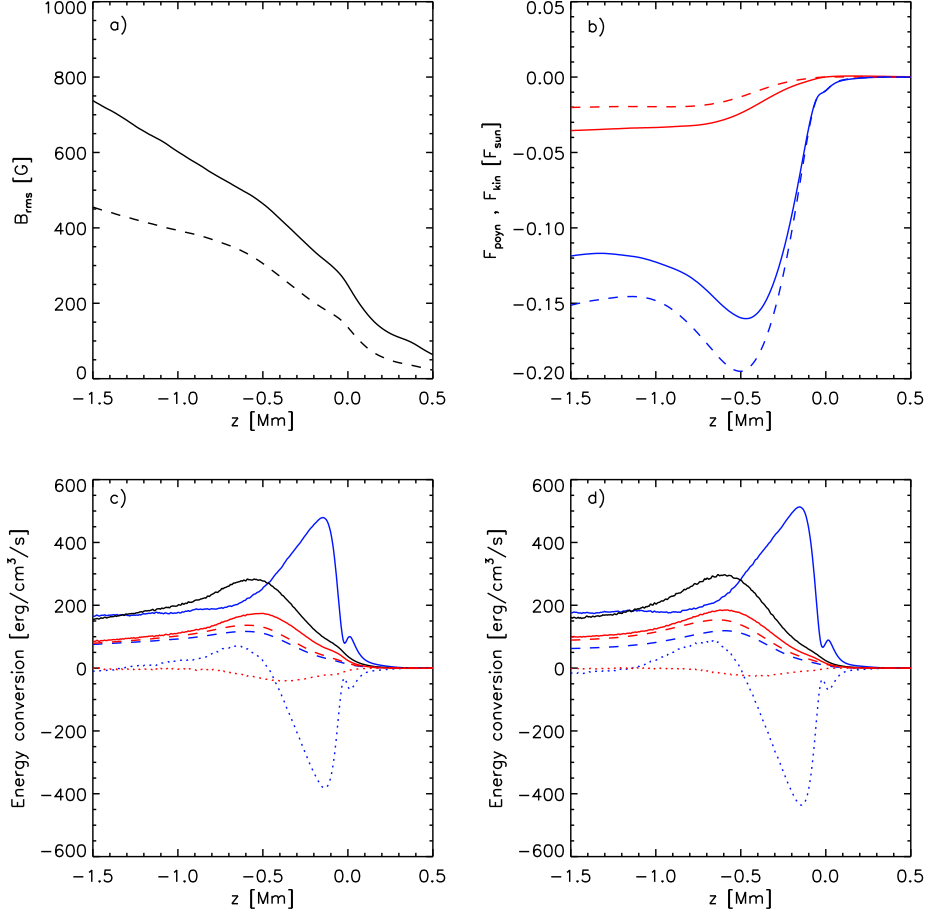


**Figure 7.** Comparison of SSD<sub>Deep</sub> and SSD<sub>Shallow</sub>: (a) RMS field strength as function of height ( $z = 0$  Mm corresponds to the average  $\tau = 1$  level) for SSD<sub>Deep</sub> (solid), SSD<sub>Shallow</sub> (dashed). (b) Poynting flux (red) and kinetic energy flux (blue) for SSD<sub>Deep</sub> (solid) and SSD<sub>Shallow</sub> (dashed). (c) Horizontally averaged energy conversion rates as function of height for SSD<sub>Deep</sub> as defined in Equations 2 and 3:  $Q_{Pres/Buo}$  (blue),  $Q_{Kin}$  (blue, dotted) and  $Q_{visc}^{NUM}$  (blue, dashed),  $-Q_{Lorentz}$  (red),  $Q_{Poynting}$  (red, dotted),  $Q_{res}^{NUM}$  (red, dashed). (d) Same as (c) for the case SSD<sub>Shallow</sub>. In (c) and (d) the solid black line shows  $Q_{Pres/Buo} + Q_{Kin}$ .

Here  $\varrho$ ,  $p$ ,  $\mathbf{v}$ , and  $\mathbf{B}$  denote mass density, pressure, velocity and magnetic field.  $\mathbf{d}_v^{NUM}$  and  $\mathbf{d}_B^{NUM}$  indicate numerical diffusion terms in the momentum and induction equation. The work by the numerical diffusion terms  $\mathbf{v} \cdot \mathbf{d}_v^{NUM}$  and  $\mathbf{B} \cdot \mathbf{d}_B^{NUM}/4\pi$  can be expressed as

$$\mathbf{v} \cdot \mathbf{d}_v^{NUM} = -\nabla \cdot [\dots] - Q_{visc}^{NUM} \quad (4)$$

$$\frac{1}{4\pi} \mathbf{B} \cdot \mathbf{d}_B^{NUM} = -\nabla \cdot [\dots] - Q_{res}^{NUM} \quad (5)$$

where the first terms on the right hand side of Equations (4) and (5) indicate viscous and resistive energy fluxes that turn out to be insignificant for the numerical diffusivities used. We use in the following discussion  $Q_{visc}^{NUM}$  and  $Q_{res}^{NUM}$  that are computed as specified in the Appendix B (see, also Rempel 2014, 2017; Hotta 2017).

Figure 7a) compares the vertical profiles of the RMS field strength in the runs SSD<sub>Deep</sub> (solid) and SSD<sub>Shallow</sub> (dashed). SSD<sub>Deep</sub> has throughout the domain a field strength that is about a factor of 1.5 – 2 stronger than SSD<sub>Shallow</sub> depending on the position. Figure 7b) compares the Poynting (red) and kinetic energy (blue) fluxes for both models. Although SSD<sub>Deep</sub> has a bottom boundary that mimics a deep convection zone by allowing transport of horizontal field into the domain in upflow regions (upward Poynting flux), that contribution is overcompensated by contributions from downflow regions, leading to an overall stronger downward directed Poynting flux. At the same time Lorentz force feedback reduces the amplitude of the downward directed kinetic energy flux, which overcompensates the contribution from the Poynting flux. These trends become even more pronounced in deeper reaching models as discussed in Hotta et al. (2015).

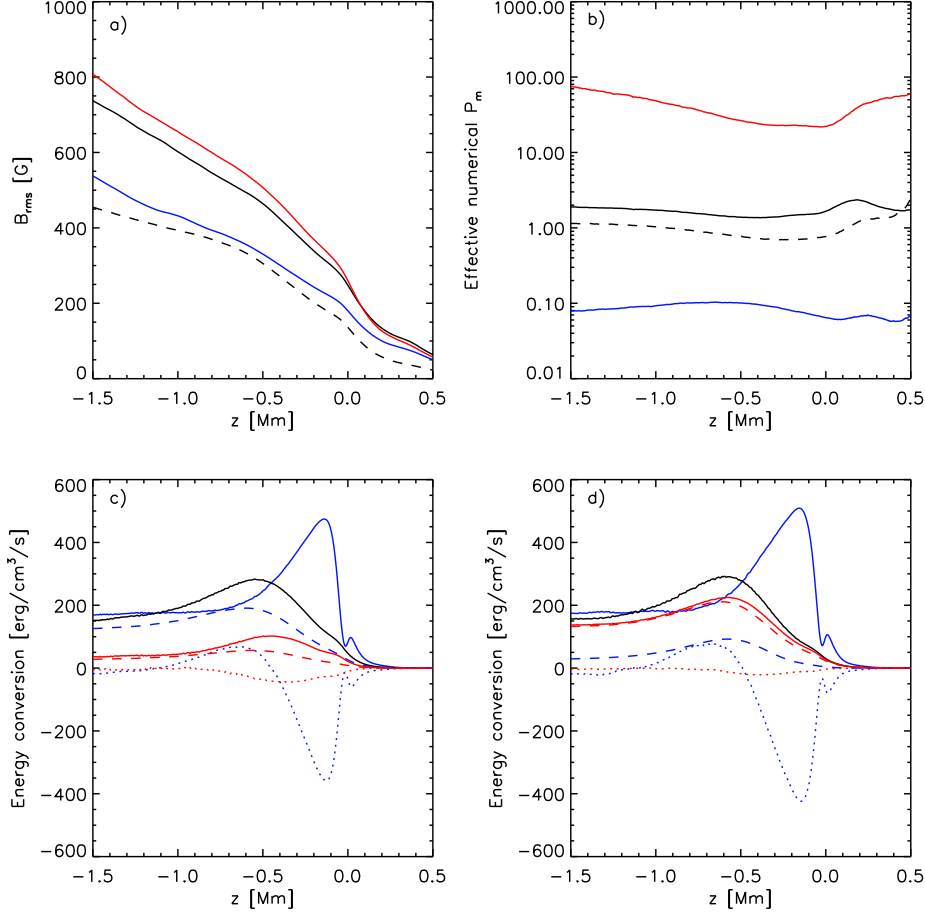


**Figure 8.** Influence of the numerical magnetic Prandtl number,  $P_m^{\text{NUM}}$ , on energy conversion rates in the simulations: (a) RMS field strength as function of height ( $z = 0$  Mm corresponds to the average  $\tau = 1$  level) for SSD<sub>Deep</sub> (solid), SSD<sub>Shallow</sub> (dashed), high  $P_m^{\text{NUM}}$  (red), low  $P_m^{\text{NUM}}$  (blue), (b) vertical profiles of  $P_m^{\text{NUM}}$  for these cases. (c) Energy conversion terms for high  $P_m^{\text{NUM}}$  case, (d) Energy conversion terms for low  $P_m^{\text{NUM}}$  case. We show the same quantities as in Figure 7(c,d).

Figure 7(c) presents an analysis of the energy conversion terms as defined in Equations (2) to (5) for the run SSD<sub>Deep</sub>. For this analysis we restarted the simulation and extracted horizontal averages of the respective terms at a high time cadence (about every 5-10 seconds) while the simulation was running for a simulated time span of about 1 hour. In particular the numerical dissipation terms  $Q_{\text{visc}}^{\text{NUM}}$  and  $Q_{\text{res}}^{\text{NUM}}$  need to be extracted directly from the simulation while it is running and cannot be computed in a post processing step (applying a filter to an already filtered solution would provide a different result). We provide the expressions for  $Q_{\text{visc}}^{\text{NUM}}$  and  $Q_{\text{res}}^{\text{NUM}}$  in the Appendix B. The primary driver (energy source) for convective motions is pressure buoyancy driving ( $Q_{\text{Pres/Buo}}$ , blue, solid) that peaks about 100 km beneath  $\tau = 1$ . Most of that driving leads to a strong downward acceleration of fluid, evident in a substantial kinetic energy flux as shown in Figure 7(b). The negative divergence of the kinetic energy flux,  $Q_{\text{Kin}}$ , is shown in Figure 7(c) as blue dotted line. The sum of  $Q_{\text{Pres/Buo}}$  and  $Q_{\text{Kin}}$  (black, solid) indicates as function of height the power that is available for sustaining turbulence against viscous dissipation as well as the small scale dynamo. This quantity peaks in a depth of 500 to 600 km beneath the photosphere. Averaged between  $z = -1.5$  Mm and  $z = 0$  Mm about 59% of  $Q_{\text{Pres/Buo}} + Q_{\text{Kin}}$  are transferred via Lorentz force work  $Q_{\text{Lorentz}}$  to magnetic energy. We show the quantity  $-Q_{\text{Lorentz}}$  (red, solid), which is the primary energy source in the magnetic energy equation. 13% of that transfer goes into the divergence of the Poynting flux,  $Q_{\text{Poynting}}$  (red, dotted), and the remainder into (numerical) resistive dissipation,  $Q_{\text{res}}^{\text{NUM}}$  (red, dashed), which has a similar magnitude as the (numerical) viscous dissipation,  $Q_{\text{visc}}^{\text{NUM}}$  (blue, dashed). Figure 7(d) shows the same terms for the run SSD<sub>Shallow</sub>. Although that simulation maintains magnetic energy at an about 3 times lower level, the overall dynamo energetics are very similar to those of SSD<sub>Deep</sub>. In order to better understand this result, we look next into the role of the effective numerical magnetic Prandtl number.

We follow here Rempel (2017) to estimate effective numerical viscosity and resistivity by comparing the numerical

viscous and resistive energy dissipation rates  $Q_{visc}^{NUM}$  and  $Q_{res}^{NUM}$  to the equivalent rates for explicit diffusivities:

$$\epsilon_\nu = \nu \varrho \sum_{i,k} \frac{\partial v_i}{\partial x_k} \left[ \frac{\partial v_i}{\partial x_k} + \frac{\partial v_k}{\partial x_i} - \frac{2}{3} \delta_{ik} \nabla \cdot \mathbf{v} \right] \quad (6)$$

$$\epsilon_\eta = \frac{\eta}{4\pi} |\nabla \times \mathbf{B}|^2 \quad (7)$$

Since numerical diffusivities are strongly intermittent and can be even zero depending on the local smoothness of the solution, a point by point comparison is not necessarily meaningful. We consider instead quantities averaged over horizontal planes, indicated by  $\langle \dots \rangle$ , leading to the effective numerical diffusivities:

$$\nu_{\text{eff}} = \frac{\langle Q_{visc}^{NUM} \rangle}{\langle \varrho \sum_{i,k} \frac{\partial v_i}{\partial x_k} \left[ \frac{\partial v_i}{\partial x_k} + \frac{\partial v_k}{\partial x_i} - \frac{2}{3} \delta_{ik} \nabla \cdot \mathbf{v} \right] \rangle} \quad (8)$$

$$\eta_{\text{eff}} = 4\pi \frac{\langle Q_{res}^{NUM} \rangle}{\langle |\nabla \times \mathbf{B}|^2 \rangle} \quad (9)$$

from which we can compute the effective numerical magnetic Prandtl number as  $P_m^{NUM} = \nu_{\text{eff}}/\eta_{\text{eff}}$  as function of height.

In addition to the runs  $\text{SSD}_{\text{Deep}}$  and  $\text{SSD}_{\text{Shallow}}$  we computed for the  $\text{SSD}_{\text{Deep}}$  setup also a high and a low  $P_m^{NUM}$  case by combining different diffusivity settings for numerical viscosity and resistivity. As described in Rempel (2014, 2017) and the Appendix B, the formulation of numerical diffusivities has a parameter  $h$  that determines how concentrated numerical diffusivities are near monotonicity changes. While we use in our standard setting  $h = 2$  for all variables, we emulate a high  $P_m^{NUM}$  case through  $h = (0, 4)$  for  $(\mathbf{v}, \mathbf{B})$ , and a low  $P_m^{NUM}$  case through  $h = (4, 0)$ . Note that this approach does not keep the magnetic Reynolds number fixed, i.e. the low  $P_m^{NUM}$  case has also the lowest value of  $R_m^{NUM}$ . The average numerical magnetic resistivity in the low  $P_m^{NUM}$  case is with  $1.6 \cdot 10^{10} \text{cm}^2 \text{s}^{-1}$  about 26 times larger than in the high  $P_m^{NUM}$  case with  $6.1 \cdot 10^8 \text{cm}^2 \text{s}^{-1}$ . Using a typical granular size of 1 Mm as length scale and a granular RMS velocity of 3 km/s as velocity scale, the corresponding  $R_m^{NUM}$  values are about 2,000 and 50,000, respectively. The former is close to the critical  $R_m^{NUM}$  found in Vögler & Schüssler (2007).

Figure 8a) shows the vertical RMS field strength for the high (red) and low (blue)  $P_m^{NUM}$  together with those for the  $\text{SSD}_{\text{Deep}}$  and  $\text{SSD}_{\text{Shallow}}$  cases from Figure 7a). The low  $P_m^{NUM}$  case has a saturation field strength almost comparable to  $\text{SSD}_{\text{Shallow}}$ , which is due to an overall lower value of  $R_m^{NUM}$ . Figure 8b) presents the  $P_m^{NUM}$  values for these cases. Depending on the location, the high  $P_m^{NUM}$  has values larger than 20, the cases  $\text{SSD}_{\text{Deep}}$  and  $\text{SSD}_{\text{Shallow}}$  between 1 and 2, and the low  $P_m^{NUM}$  case around 0.1.

Figure 8c) and 8d) show the energy conversion terms for the high and low  $P_m^{NUM}$  case, respectively. As discussed by Brandenburg (2011, 2014) we find also here with purely numerical diffusivities that  $P_m^{NUM}$  controls the ratio between  $Q_{visc}^{NUM}$  and  $Q_{res}^{NUM}$ , which is about 3 for the high  $P_m^{NUM}$  and about 0.3 for the low  $P_m^{NUM}$  case, note that the latter has at the same time the lower saturation field strength. Although the cases  $\text{SSD}_{\text{Deep}}$  and  $\text{SSD}_{\text{Shallow}}$  use the same numerical diffusivity settings, they differ in their value of  $P_m^{NUM}$  by about a factor of 2, with  $\text{SSD}_{\text{Shallow}}$  having the lower value.  $\text{SSD}_{\text{Shallow}}$  has a slightly lower  $P_m^{NUM}$  as  $\text{SSD}_{\text{Deep}}$  since magnetic field in  $\text{SSD}_{\text{Shallow}}$  is organized on smaller scales than in  $\text{SSD}_{\text{Deep}}$  and is consequently more strongly affected by numerical dissipation terms. The similar energy conversion rates in  $\text{SSD}_{\text{Deep}}$  and  $\text{SSD}_{\text{Shallow}}$  (Figure 7) are a consequence of comparable effective numerical magnetic Prandtl numbers within a factor of 2.

Overall our findings are consistent (at least on a qualitative level) with those reported by Brandenburg (2011, 2014) using simulations of forced turbulence with explicit viscosity and magnetic diffusivity. For our lowest value of  $P_m^{NUM} \sim 0.1$  we find that  $Q_{\text{Lorentz}}$  is about 80% of  $Q_{\text{Pres/Buo}} + Q_{\text{Kin}}$ , whereas it is only 30% in the high  $P_m^{NUM}$  case. Assuming that this scaling extends to  $P_m$  values as low as  $10^{-5}$  found in the solar photosphere, it is conceivable that  $Q_{\text{Lorentz}}$  would reach close to 100% of  $Q_{\text{Pres/Buo}} + Q_{\text{Kin}}$ , i.e. Maxwell-stresses take over the role of Reynolds-stresses and viscous dissipation becomes insignificant. Integrated over the uppermost 1.5 Mm of the convection zone  $Q_{\text{Pres/Buo}} + Q_{\text{Kin}}$  reaches in the simulation  $\text{SSD}_{\text{Deep}}$  a value of 46% of the solar luminosity (the other cases considered are within a few % of this value), i.e. the energy conversion by the small-scale dynamo is expected to be quite substantial.

#### 4. CONCLUSIONS

We analyzed the magnetic field amplification in exploding granules and focused in particular on the time evolution of newly formed downflow lanes. We found the following sequence of events in at least four exploding granules present



in the analyzed simulation run  $\text{SSD}_{\text{Deep}}$ :

1. Horizontal flows converging towards the newly forming downflow lane amplify a weak (a few 10 G) field present in granular upflows to a strength exceeding 800 G within a time span of a few minutes. The newly forming downflow lane remains mostly laminar, i.e. field amplification due to turbulent velocity shear remains weak.
2. The newly forming downflow lane develops asymmetric horizontal vorticity, which is manifest early on in the intensity image in form of sharp intensity gradients on one side of the downflow lane (Steiner et al. 2010).
3. Within a few minutes magnetic field with a more turbulent appearance becomes visible at the edge of the adjacent granule that showed previously the sharper intensity gradients. The turbulent magnetic field is swept into the downflow lane and leads to the presence of turbulent field (and flows) in the newly formed downflow lane.

In the early stages of this process vertical magnetic field is primarily amplified by horizontally converging flows, which is an unavoidable consequence of overturning granular motions. This term is strong enough to produce narrow sheets of vertical field reaching more than 800 G in a few minutes. The structure of these sheets in terms of extent along the downflow lane as well as polarity (some sheets are unipolar, whereas others may have mixed polarity) is a reflection of the structure in the granular seed field. Since plasma that appears in the center of granules has undergone substantial horizontal expansion, magnetic field in the center of granules tends to be organized on scales comparable to the granular extent. Thus studying the structure of magnetic field in newly forming downflow lanes provides a way to quantify the strength and structure of magnetic field that reaches the photosphere from the deeper convection zone. This deep recirculation component provides a significant contribution to small-scale magnetism in the photosphere. The simulation  $\text{SSD}_{\text{Shallow}}$  that assumes  $\mathbf{B} = 0$  G in upflows at the bottom boundary has an about 1.5 – 2 times lower saturation level. Such values falls short in comparison with observations (Danilovic et al. 2010, 2016). In addition to that the sheet-like organization of magnetic field is less pronounced.

We did focus our discussion mostly on exploding granules since they provide the most undisturbed view on the field amplification process, the described picture is however representative for the photosphere as a whole.

We note that current simulations might not properly capture the structure of the deep recirculation component. On the one hand, the finite domain depth underestimates the smoothing due to horizontal expansion; on the other hand, the finite grid spacing imposes a lower limit to the scale of magnetic field at the bottom boundary, which becomes amplified due to horizontal expansion. Addressing this problem in simulations requires the combination of deeper domains with higher resolution, which is numerically expensive. Therefore observational constraints from current and future high resolution telescopes are required for further progress.

Interestingly, the total energy conversion associated with small-scale dynamo action is not affected by the presence or absence of deep recirculation. We find in both  $\text{SSD}_{\text{Deep}}$  and  $\text{SSD}_{\text{Shallow}}$  comparable amounts of work against the Lorentz force in spite of different saturation field strengths. As previously discovered by Brandenburg (2011, 2014) we also find that the magnetic Prandtl number (in our case the effective numerical magnetic Prandtl number,  $P_m^{\text{NUM}}$ ) determines the overall energy conversion through the Lorentz force/induction terms and consequently the ratio of viscous to resistive energy conversion. For a value of  $P_m^{\text{NUM}} \sim 0.1$ ,  $Q_{\text{Lorentz}}$  is about 80 % of  $Q_{\text{Pres/Buo}} + Q_{\text{Kin}}$  (local convective driving), which translates to more than 30 % of the solar luminosity when integrated over the uppermost 1.5 Mm of the convection zone. Assuming that this scaling extends to  $P_m$  values as low as the  $10^{-5}$  found in the solar photosphere,  $Q_{\text{Lorentz}}$  could be close to 100 % of  $Q_{\text{Pres/Buo}} + Q_{\text{Kin}}$ . In the presented simulations Maxwell-stresses are of substantial strength and take over the role of Reynolds stresses and viscous dissipation. While less clear in the near surface layers, this does influence the structure of convection of turbulence in deeper simulations domains as demonstrated by Hotta et al. (2015). They compare pure hydrodynamic and small-scale dynamo simulations and found in the latter a reduction of the upflow/downflow mixing somewhat similar to high thermal Prandtl number convection, which is expected at least on a qualitative level when the Maxwell-stress mimics the effect of turbulent stresses.

We do not find strong *direct* evidence for turbulent field amplification in the *visible* layers of the photosphere. Turbulent field appears first in granular upflows near the edge of granules, indicating subsurface field amplification and shallow recirculation. Overall our analysis shows that small-scale field in the visible layers of the photosphere has two distinct contributions that can be linked to shallow and deep recirculation. Shallow recirculation provides the primary source for field with turbulent appearance on small scales, whereas deep recirculation can be linked to strong sheet-like field structures in downflow lanes that do have a coherence comparable to the extent of granules. Models with only shallow recirculation ( $\text{SSD}_{\text{Shallow}}$ ) fall short by about a factor of 1.5 – 2 compared to observations,

whereas models with deep recirculation (SSD<sub>Deep</sub>) do match observational constraints. High resolution observations of the deep photosphere could provide valuable constraints on the relative contribution from these two processes. In both cases the total energy conversion by Maxwell stresses is substantial.

The National Center for Atmospheric Research (NCAR) is sponsored by the National Science Foundation. The author thanks Valentin Martinez-Pillet, Rebecca Centeno-Elliott and the anonymous referee for valuable comments on the manuscript. High-performance computing resources were provided by NCAR’s Computational and Information Systems Laboratory, sponsored by the National Science Foundation, on Yellowstone (<http://n2t.net/ark:/85065/d7wd3xhc>) and Cheyenne (doi:10.5065/D6RX99HX).

## REFERENCES

- Boldyrev, S., & Cattaneo, F. 2004, *Physical Review Letters*, 92, 144501
- Brandenburg, A. 2011, *ApJ*, 741, 92
- . 2014, *ApJ*, 791, 12
- Buehler, D., Lagg, A., & Solanki, S. K. 2013, *A&A*, 555, A33
- Bushby, P. J., & Favier, B. 2014, *A&A*, 562, A72
- Cattaneo, F. 1999, *ApJ*, 515, L39
- Danilovic, S., Rempel, M., van Noort, M., & Cameron, R. 2016, *A&A*, 594, A103
- Danilovic, S., Schüssler, M., & Solanki, S. K. 2010, *A&A*, 513, A1
- Hotta, H. 2017, *ApJ*, 845, 164
- Hotta, H., Rempel, M., & Yokoyama, T. 2015, *ApJ*, 803, 42
- Ishikawa, R., & Tsuneta, S. 2009, *A&A*, 495, 607
- Iskakov, A. B., Schekochihin, A. A., Cowley, S. C., McWilliams, J. C., & Proctor, M. R. E. 2007, *Physical Review Letters*, 98, 208501
- Khomenko, E., Vitas, N., Collados, M., & de Vicente, A. 2017, *A&A*, 604, A66
- Kitiashvili, I. N., Kosovichev, A. G., Mansour, N. N., & Wray, A. A. 2015, *ApJ*, 809, 84
- Lamb, D. A., Howard, T. A., & DeForest, C. E. 2014, *ApJ*, 788, 7
- Lites, B. W. 2011, *ApJ*, 737, 52
- Lites, B. W., Centeno, R., & McIntosh, S. W. 2014, *PASJ*, 66, S4
- Petrovay, K., & Szakaly, G. 1993, *A&A*, 274, 543
- Pietarila Graham, J., Cameron, R., & Schüssler, M. 2010, *ApJ*, 714, 1606
- Rempel, M. 2014, *ApJ*, 789, 132
- . 2017, *ApJ*, 834, 10
- Schekochihin, A. A., Haugen, N. E. L., Brandenburg, A., et al. 2005, *ApJL*, 625, L115
- Schekochihin, A. A., Iskakov, A. B., Cowley, S. C., et al. 2007, *New Journal of Physics*, 9, 300
- Stein, R. F., Bercik, D., & Nordlund, Å. 2003, in *Astronomical Society of the Pacific Conference Series*, Vol. 286, *Current Theoretical Models and Future High Resolution Solar Observations: Preparing for ATST*, ed. A. A. Pevtsov & H. Uitenbroek, 121
- Steiner, O., Franz, M., Bello González, N., et al. 2010, *ApJL*, 723, L180
- Thaler, I., & Spruit, H. C. 2015, *A&A*, 578, A54
- Tobias, S. M., Cattaneo, F., & Boldyrev, S. 2013, in *Ten Chapters in Turbulence*, ed. P. A. Davidson, Y. Kaneda, & K. R. Sreenivasan (Cambridge: Cambridge Univ. Press), 351–404
- Vögler, A., & Schüssler, M. 2007, *A&A*, 465, L43

## APPENDIX

### A. ADDITIONAL EXAMPLES OF EXPLODING GRANULES

Figures 9, 10, and 11 show quantities similar to Figure 1 for three additional examples of exploding granules. These examples show the same sequence of events: (1) amplification of vertical magnetic field due to convergent horizontal flows leading to concentrated magnetic sheets, (2) asymmetric horizontal vorticity leading to a bright edge on one side of the newly formed downflow lane, (3) turbulent magnetic field appearing in the granular upflow on the edge that showed previously the brighter intensity.

### B. NUMERICAL DIFFUSIVITIES

We provide a description of numerical diffusivities and computation of viscous and resistive heating as given in Rempel (2014, 2017). For simplicity we consider here only a one-dimensional problem. The computation of numerical diffusivities is performed in a dimensional split fashion, i.e. contributions from the 3 grid directions are added sequentially. The first step is a piece linear reconstruction of the solution  $u$  leading extrapolated values at cell interfaces given by

$$u_l = u_i + 0.5 \Delta u_i \quad (\text{B1})$$

$$u_r = u_{i+1} - 0.5 \Delta u_{i+1} . \quad (\text{B2})$$

The scheme is applied to the variables  $u = \{\log(\varrho), v_x, v_y, v_z, \log \varepsilon, B_x, B_y, B_z\}$ , where  $\varepsilon$  is the internal energy per unit mass. Here  $u_l$  ( $u_r$ ) are the extrapolated values from cells on the left (right), the reconstruction slope  $\Delta u_i$  is computed

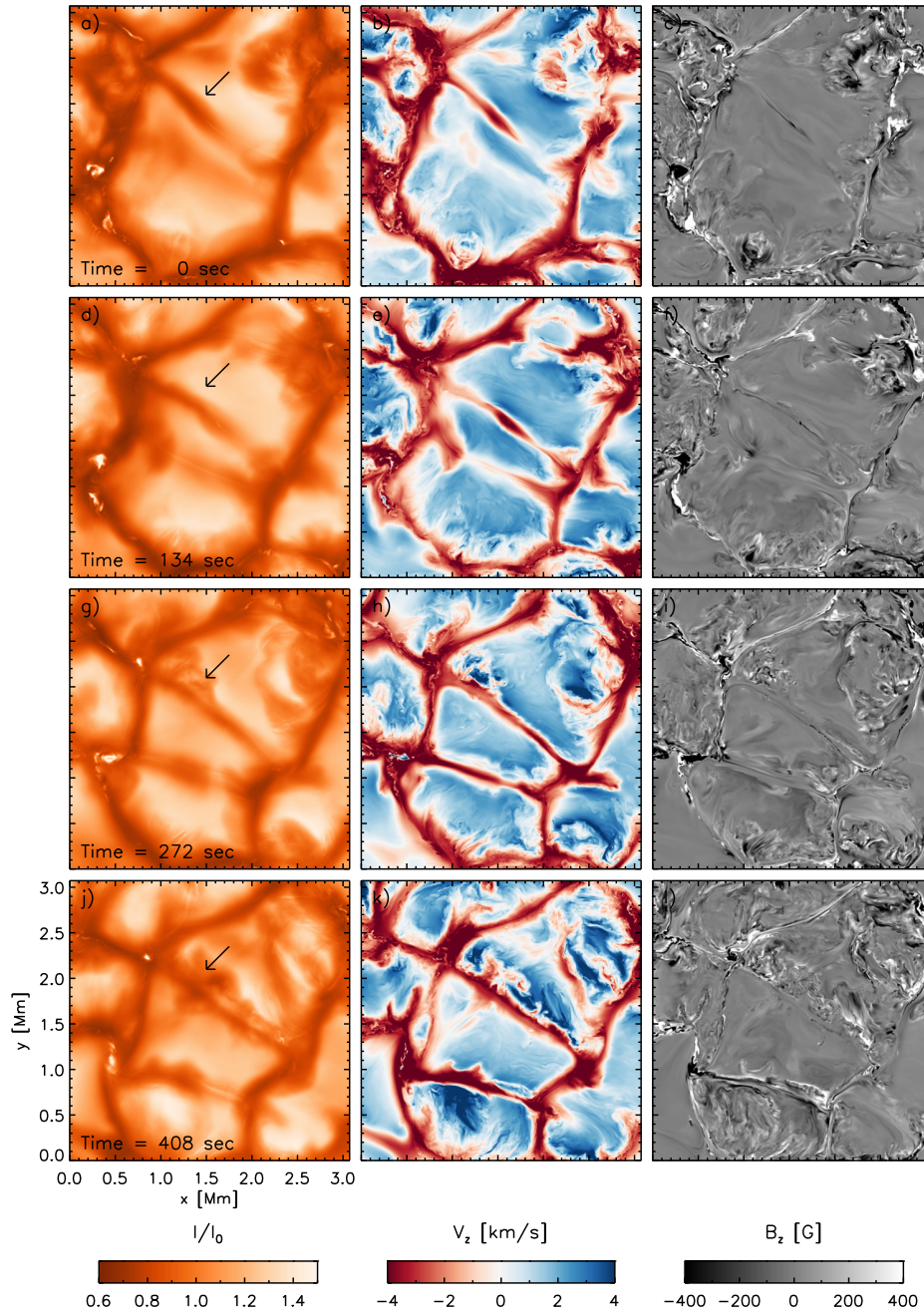


Figure 9. Same as Figure 1 for a different case.

using the monotonized central difference limiter:

$$\Delta u_i = \text{minmod} [(u_{i+1} - u_{i-1})/2, 2(u_{i+1} - u_i), 2(u_i - u_{i-1})] . \quad (\text{B3})$$

Numerical diffusive fluxes at cell interfaces are computed from the extrapolated values through the expression

$$f_{i+\frac{1}{2}}^{\text{NUM}} = -\frac{1}{2} c_{i+\frac{1}{2}} \Phi_h(u_r - u_l, u_{i+1} - u_i) \cdot (u_r - u_l) , \quad (\text{B4})$$

where  $c_{i+\frac{1}{2}}$  is the characteristic velocity at the cell interface. In the simulations presented here we use  $c = |\mathbf{v}| + \sqrt{(0.2 C_S)^2 + V_A^2}$ . The function  $\Phi_h$  allows to further control the (hyper-) diffusive character of the scheme, it is given



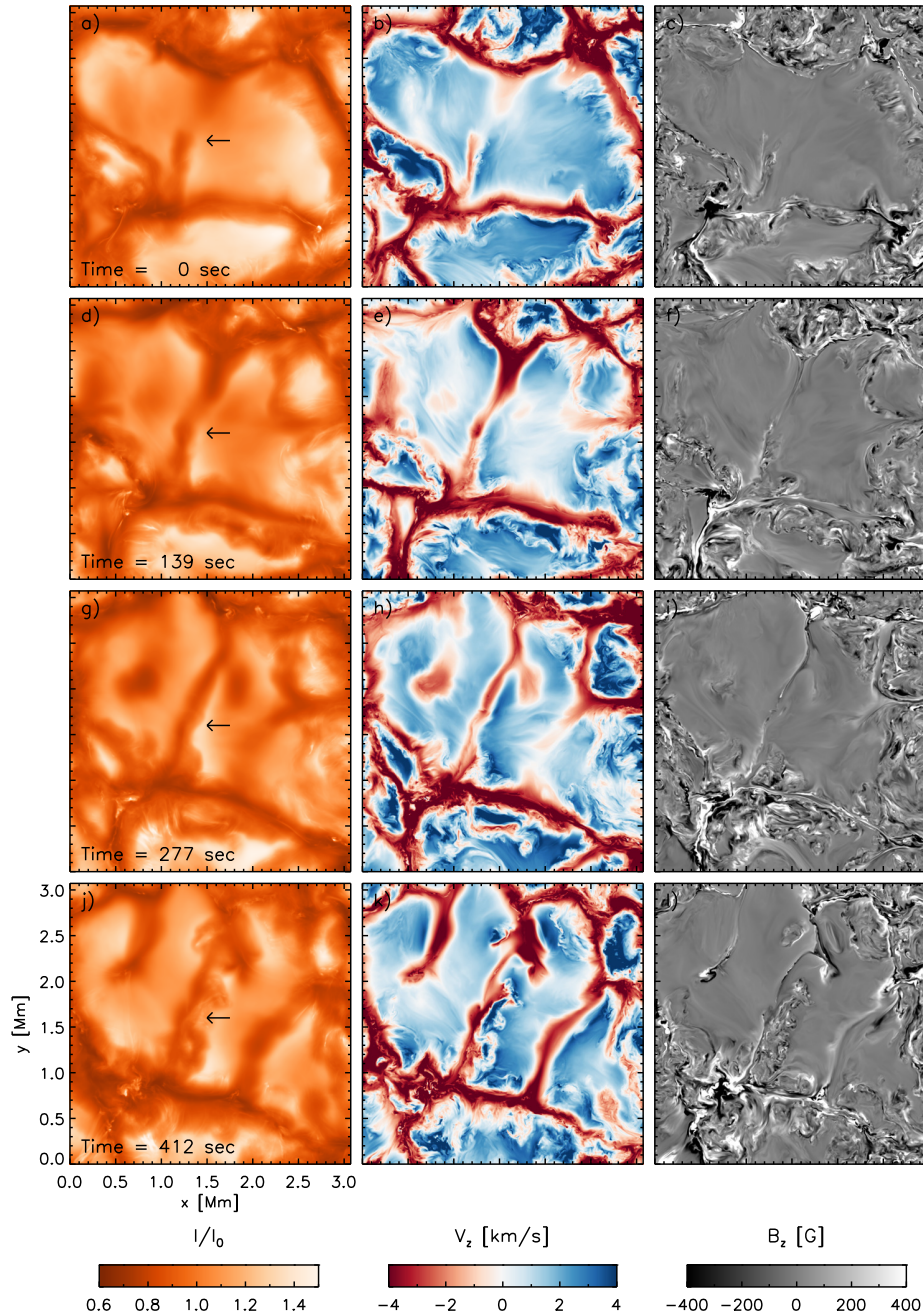


**Figure 10.** Same as Figure 1 for a different case.

by

$$\Phi_h = \max \left[ 0, 1 + h \left( \frac{u_r - u_l}{u_{i+1} - u_i} - 1 \right) \right] \quad (\text{B5})$$

in regions with  $(u_r - u_l) \cdot (u_{i+1} - u_i) > 0$ , while  $\Phi_h = 0$  if  $(u_r - u_l) \cdot (u_{i+1} - u_i) \leq 0$  (no anti-diffusion). For  $h = 0$  the scheme reduces the diffusive flux to that of a standard second order Lax-Friedrichs scheme, while for  $h > 0$  the diffusivity is reduced for smooth regions in which  $|(u_r - u_l)/(u_{i+1} - u_i)| < 1$ . Some additional contributions from a 4<sup>th</sup> order hyper-diffusion as well as correction terms for mass diffusion as detailed in Rempel (2014) are added, but their contributions are insignificant and not explicitly spelled out here.

Applying the scheme to the velocity  $v_i^m$  and magnetic field  $B_i^m$  variables ( $i$  denotes the grid position, whereas  $m = 1, 2, 3$  the vector components) leads to the following expressions for numerical viscous and resistive heating:



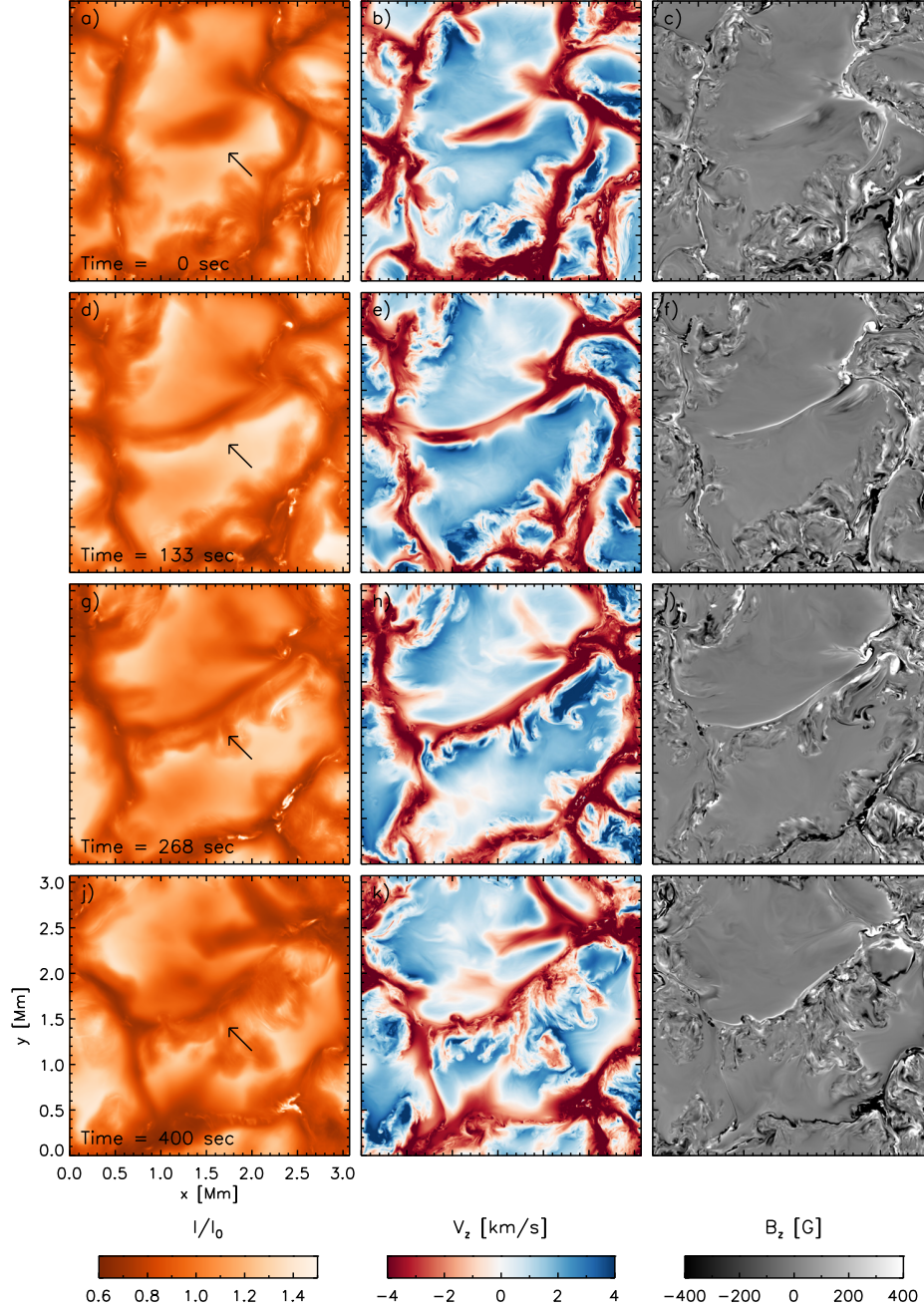


Figure 11. Same as Figure 1 for a different case.

$$(Q_{visc}^{\text{NUM}})_i = \frac{1}{2} \rho_i \sum_{m=1}^3 \left[ (f_v^{\text{NUM}})^m_{i-\frac{1}{2}} \frac{v_i^m - v_{i-1}^m}{\Delta x} + (f_v^{\text{NUM}})^m_{i+\frac{1}{2}} \frac{v_{i+1}^m - v_i^m}{\Delta x} \right] \quad (\text{B6})$$

$$(Q_{res}^{\text{NUM}})_i = \frac{1}{8\pi} \sum_{m=1}^3 \left[ (f_B^{\text{NUM}})^m_{i-\frac{1}{2}} \frac{B_i^m - B_{i-1}^m}{\Delta x} + (f_B^{\text{NUM}})^m_{i+\frac{1}{2}} \frac{B_{i+1}^m - B_i^m}{\Delta x} \right]. \quad (\text{B7})$$